



Forced separation unsteadiness in a supersonic blunt fin flow

Haryl Ngoh ^{*} and Jonathan Poggie [†]*Purdue University, West Lafayette, Indiana 47907, USA*

(Received 24 February 2022; revised 27 July 2022; accepted 24 August 2022; published 12 September 2022)

Detached eddy simulations of a Mach 3, turbulent flow over a blunt fin were performed. Past experiments have shown that this configuration generates a large, three-dimensional, unsteady, separated region. Our previously published detached eddy simulations exhibited large-scale unsteadiness even in the absence of fluctuations in the incoming flow. The introduction of synthetic turbulence at the inflow boundary altered that separation motion. With the previous simulations as a reference baseline, a parametric study was carried out of the response of the flow to time-periodic forcing of the incoming boundary layer. The disturbances were introduced into the boundary layer through momentum and energy source terms. The spatial form of the source terms was based on averages of the baseline flow, conditioned on the motion of the separation shock. The response of the separation shock motion to the imposed perturbations was found to be dependent on the frequency of forcing. With a forcing frequency representative of the characteristic large-scale separation unsteadiness in the baseline flow, the separation shock motion was phase locked to the applied force, and a larger forcing amplitude led to greater separation motion. The separation region did not, however, respond strongly to disturbances in a higher frequency range. These results show that, in a flow that oscillates in the absence of upstream disturbances, separation motion can be modulated by upstream forcing of a particular form. Similar results have been obtained in the past for flows where separation unsteadiness is directly driven by incoming turbulence, but the modulation of self-excited oscillations in the present class of flow is a different behavior. It suggests opportunities for flow control of strong shock-wave–boundary-layer interactions.

DOI: [10.1103/PhysRevFluids.7.093903](https://doi.org/10.1103/PhysRevFluids.7.093903)

I. INTRODUCTION

Shock-wave/boundary-layer interactions complicate the design of air vehicles in the transonic and supersonic speed regimes, increasing both drag and thermomechanical loading. One of the most significant design concerns is large-scale separation unsteadiness, leading to cyclic loading in a low-frequency range. Such concentrated mechanical and thermal loads can produce a strong structural response and promote fatigue failure [1]. Better understanding of these processes could lead to less conservative design, lower drag, lighter aircraft, and a corresponding improvement in fuel efficiency. Research that explores separation unsteadiness in shock-wave–boundary-layer interactions is thus of strong practical interest.

A. Separation unsteadiness

Shock-wave–boundary-layer interaction is often associated with three-dimensional, unsteady, separated flow. Unsteadiness with a characteristic frequency much lower than that of the boundary

^{*}jngoh@purdue.edu

[†]jpoggie@purdue.edu

layer turbulence has been reported for interactions corresponding to a variety of geometries and flow conditions [1–5]. To achieve successful flow control, therefore, it is imperative to understand the origin and nature of this unsteadiness.

A variety of instabilities or other mechanisms may ultimately generate the unsteadiness, but from the flow control perspective, the separation region can be treated as a black box that generates large-scale, low-frequency motion. As such, the separation region can either amplify external disturbances (amplifier), oscillate on its own (oscillator), or be governed by a borderline case of weakly damped oscillations (resonator). Previous work by our research group has focused on the resonator case of a weak compression ramp interaction [6,7]. In that case, separation motion was linked to disturbances in the incoming boundary layer. More recently, Ngoh and Poggie [8] studied a blunt fin interaction, and they showed that oscillations appear even in the absence of fluctuations in the incoming boundary layer (oscillator case). The blunt fin case can be expected to differ from the compression ramp flow, given the stronger shock waves, larger separation region, and greater three dimensionality of the blunt fin flow. Nonetheless, when synthetic turbulence was introduced in the incoming flow, a detectable difference in the separation unsteadiness was found. The blunt fin flow is both affected by self-excited oscillations and responsive to incoming disturbances. This responsiveness offers an opportunity for flow control.

B. Flow control

Flow control methods are generally classified as passive or active. Passive flow control methods are attractive because they do not require input energy, but their range of operation is commonly narrow and limited to on-design conditions. Examples of passive flow control methods include vortex generators [9–11], other surface geometry perturbations [12,13], and passive blowing–suction configurations based on a perforated plate over a cavity [14–16]. Some reduction of the extent of boundary-layer flow separation and shock-wave–boundary-layer interaction unsteadiness has been achieved through these methods.

Active flow control methods offer potentially versatile solutions that can adjust to local flow conditions, at the cost of energy input. Air jets, active surface morphing, laser energy deposition, and plasma actuators have all been considered for use as active flow control devices, and they have been the focus of experimental and numerical studies. Experimental studies of micro–air-jet actuators have demonstrated reduction in boundary-layer separation length, pressure loads, and shock unsteadiness [17–20]. The injected jets altered the overall structure of the shock system and generated vortices, which energized the boundary layer upstream of the interaction.

Through direct numerical simulations, Shinde *et al.* [12] showed that active surface morphing could prevent transition and reduce separation extent, as well as the associated unsteadiness, for a transitional shock-wave–boundary-layer interaction. Lee and Gross [13] used large-eddy simulations to explore the effects of a corrugated wall on a reflected shock-induced interaction flow, and they found that the low-frequency unsteadiness of the separation motion was modified. Recent experimental studies of the fluid-structure interaction between a compliant panel and a compression ramp-induced flow by Eitner *et al.* [21] showed that the unsteadiness of the separation shock foot was influenced by the vibration modes of the panel. Energy deposition through laser sources can alter the shock structure through local changes in flow density [22–25]. Some success in alleviating shock unsteadiness has been demonstrated [25], but the cost of increased heat transfer must be carefully considered [22].

A variety of plasma-based flow control methods have been developed, including arc filament plasma actuators [26–31], pulsed plasma jet actuators [32–34], dielectric barrier discharge plasma actuators [35], and magnetically driven surface discharge actuators [36–39]. Depending on the specific actuator design, the shock-wave–boundary-layer interaction may be influenced through different mechanisms. Heating of the boundary-layer flow tends to increase the separation length due to a decrease in the local Mach number [32] or increase in boundary-layer displacement thickness [28]. In contrast, vorticity generation may increase turbulent mixing and decrease separation length

[32,34,35]. The shock system may also be altered sufficiently to replace the strong separation shock with several weak compression waves, reducing the intensity of fluctuations at the wall [29–31]. Through an applied magnetic field, the surface plasma may be manipulated to impose an upstream or downstream force on the flow, affecting the shock-wave–boundary-layer interaction characteristics [36–39].

Active flow control of both swept fin and compression ramp-induced interactions has been achieved using pulsed microjets. The separation shock motion of the three-dimensional interaction over a swept fin is characterized by midfrequency unsteadiness (one decade above the typical low-frequency unsteadiness found in other interactions). Midfrequency forcing via pulsed microjets at various positions within the interaction region [40,41] showed that the separation shock motion was more responsive to perturbations introduced upstream of the separation, as opposed to near reattachment. With upstream forcing, the separation shock motion was phase matched to the unsteady perturbations. For a compression ramp-induced interaction, control of the low-frequency unsteadiness of the separation shock through upstream perturbations has been demonstrated both experimentally [33] and computationally [7]. With the perturbation frequency set around the peak low-frequency unsteadiness, the separation motion was locked onto the imposed perturbations. Similar effects have been demonstrated in subsonic separated flow [42].

C. Present work

The motivation of the present work is to investigate whether similar control of low-frequency unsteadiness can be achieved for a blunt fin interaction, which represents an interaction of larger separation scale, greater three dimensionality, and a stronger separation shock. The blunt fin flow displays strong streamline curvature near separation and reattachment, and thus possibly an instability that drives self-induced separation oscillations [43].

Indeed, our previously published detached eddy simulations [8] of this flow exhibited large-scale unsteadiness even in the absence of fluctuations in the incoming flow. For such a flow, a weak response to external forcing might be expected in the presence of the strong internal growth of perturbations within the recirculation region [44,45]. Nonetheless, we found that the introduction of synthetic turbulence at the inflow boundary altered the separation motion.

With the previous simulations [8] as a reference baseline, a parametric study was carried out in the present work of the response of the flow to time-periodic forcing of the incoming boundary layer. The disturbances were introduced into the boundary layer through momentum and energy source terms. The spatial form of the source terms was based on averages of the baseline flow, conditioned on the motion of the separation shock. With future flow control applications in mind, an aim of this study was to introduce a small, unsteady perturbation in the incoming flow with a relatively small effect on the mean-flow characteristics.

II. METHODS

Detached eddy simulations were performed for a turbulent blunt fin flow at Mach 3. The calculations were performed on the Brown computing cluster at Purdue University’s Rosen Center for Advanced Computing [46]. The conditions were chosen to match well-known experiments by Dolling and co-workers [47,48]. Our previous calculations [8] demonstrated that the computational approach can accurately predict the experimental results for the baseline flow.

A. Baseline computational setup

The open-source computational fluid dynamics software SU2 was used to perform the flow calculations [49,50]. In previous work, detached eddy simulations with this code were shown to adequately predict the shock-wave–boundary-layer interaction induced by a blunt fin [8]. In particular, the predicted mean, root-mean-square, and power spectral density of the wall pressure

TABLE I. Incoming flow conditions.

Parameter	Value
Freestream Mach number, M_∞	3.0
Freestream stagnation temperature, T_0 (K)	260
Freestream stagnation pressure, P_0 (Pa)	6.8×10^5
Freestream unit Reynolds number, Re_∞ (m^{-1})	6.5×10^7
Fin thickness, D (mm)	12.7
Boundary layer thickness, δ_0 (mm)	3.3

fluctuations agreed with the experimental measurements within measurement error and statistical uncertainty.

The ideal-gas, compressible Navier-Stokes equations were solved numerically using the finite-volume method on an unstructured computational mesh. The convective fluxes for the Navier-Stokes equations were discretized using the Jameson-Schmidt-Turkel numerical scheme, and the turbulence transport equation was discretized with a first-order upwind scheme. An implicit second-order dual time-stepping method was used to solve the unsteady equations. The linear system was solved iteratively using the flexible generalized minimum residual method with an incomplete lower upper factorization (ILU) preconditioner.

A hybrid Reynolds-averaged Navier-Stokes–large-eddy simulation (RANS–LES) method known as enhanced delayed detached eddy simulation was employed to treat the flow turbulence [51]. In near-wall regions or attached boundary-layer flow, the effect of turbulence was modeled through a turbulent viscosity term via the Spalart-Allmaras turbulence model [52]. In regions of flow separation or away from walls, the turbulent viscosity was reduced so that it acted like a subgrid-scale model in a large-eddy simulation. The switch between modeled and resolved turbulence was controlled by a shear layer adapted subgrid-length scale that is a function of the local flow variables as well as by grid spacing in the three dimensions.

The incoming flow conditions (see Table I) and computational grid were the same as that of our previous study [8]. The computational domain represents a blunt fin mounted on a flat plate (see Fig. 1). The x , y , and z coordinates refer to the streamwise, spanwise, and wall-normal directions, respectively. The origin was located at the root of the blunt fin leading edge. A supersonic inlet boundary condition was applied at the inflow boundary ($x/D = -4.33$). A turbulent boundary-

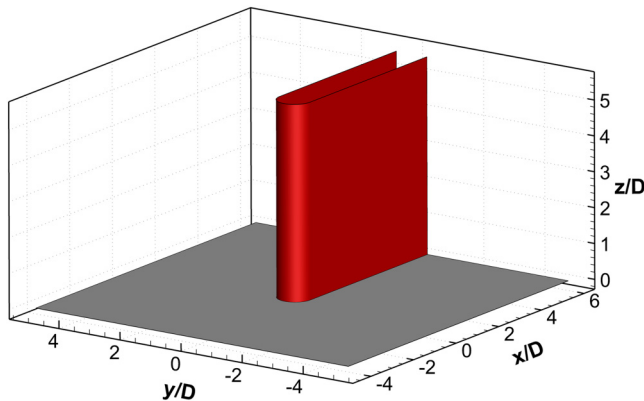


FIG. 1. Computational domain. The red surface represents the fin wall, and the gray surface represents the plate wall. The inlet and outlet boundaries are omitted for clarity.

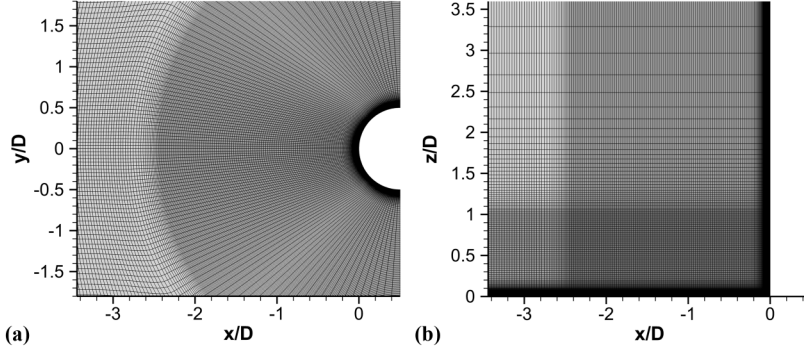


FIG. 2. Computational mesh: (a) top view, (b) side view.

layer mean-flow profile (obtained from a separate flat-plate boundary-layer RANS calculation), with synthetically generated unsteady turbulent perturbations (via a digital filter method) was imposed at the inlet. The wall surfaces of the plate and fin were defined with an adiabatic, no-slip boundary condition. The remaining boundaries of the domain were set as supersonic outlets.

The grid was refined in the shock-wave–boundary-layer interaction region (near the root of the blunt fin). Within the resolved region around the separation and the lambda shock, the wall-normal resolution ranges from $0.2 < \Delta z^+ < 0.8$ at the wall ($z/D = 0$) to $75 < \Delta z^+ < 300$ at the upper edge of the shock-wave–boundary-layer interaction region (about $z/D = 1.0$). Inside this region, the streamwise resolution was $60 < \Delta x^+ < 250$ and the spanwise resolution was $140 < \Delta y^+ < 400$. The total number of cells in the computational mesh was 13×10^7 (see Fig. 2).

The time step was $\Delta t = 0.25 \mu\text{s}$. The corresponding nondimensional time step $\Delta t^+ = u_\tau^2 \Delta t / \nu_w$ ranged from 1.3 to 11 inside the interaction region ($x/D > -2.5$). Alternatively, $U_\infty \Delta t / \delta_0 = 0.044$ and $U_\infty \Delta t / (2.5D) = 0.0046$.

B. Forcing function

Streamwise forcing of the flow was implemented as a momentum source term f_x (an artificial body force), and an associated energy source term uf_x (rate of work done by the artificial body force) in the flow equations [49,53]. The function describing the force is shown in Eq. (1). The design process of this forcing function was similar to that employed by Poggie [7] in a study of forcing on a compression ramp-induced shock-wave–boundary-layer interaction flow.

$$f_x = Af(x)g(z) \cos(2\pi f_0 t), \quad (1)$$

$$f(x) = \frac{\exp(-X^2)}{\sqrt{\pi}x_r}, \quad (1a)$$

$$g(z) = \frac{[\exp(-\frac{Z}{a})]\{d + \cos[\pi(\frac{Z}{c} - b)]\}}{adz_r + \frac{z_r[ac^2 \cos(\pi b) + a^2 c \pi \sin(\pi b)]}{c^2 + a^2 \pi^2}}, \quad (1b)$$

$$X = \frac{x - x_1}{x_r}, \quad (1c)$$

$$Z = \frac{z}{z_r}. \quad (1d)$$

Here, A and f_0 denote the forcing amplitude and frequency, respectively. The parameter x_1 is the location of the center of the source term in the streamwise direction. The parameters x_r and z_r are the length scales of the function in the streamwise and wall-normal directions, respectively. This function represents a force density that is sinusoidally periodic in time. At a given instant, the

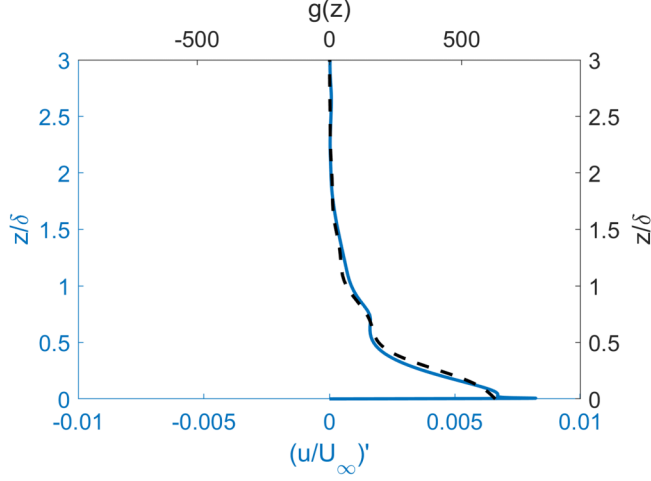


FIG. 3. Comparison of forcing function wall-normal shape (broken line) and conditionally averaged streamwise velocity profile (continuous line).

magnitude of the force is uniform in the spanwise (y) direction, and it diminishes exponentially in the streamwise (x) direction from the source origin.

In a previous study of the baseline (without forcing) blunt fin-induced shock-wave–boundary-layer interaction, strong correlation was found between the perturbations in the streamwise velocity of the incoming boundary-layer flow and the perturbations in separation shock velocity. Conditional averages of the incoming streamwise flow velocity based on the separation shock velocity magnitude and direction revealed a characteristic velocity profile [8].

For this study, the shape of the forcing function in the wall-normal (z) direction $g(z)$ was chosen to match the characteristic velocity profile (see Fig. 3). The functions $f(x)$ and $g(z)$ were normalized such that the integrals over the domain were unity ($\int_{-\infty}^{\infty} f(x)dx = 1$ and $\int_0^{\infty} g(z)dz = 1$). The source origin was placed at $x_1/D = -3.5$, in the undisturbed boundary layer upstream of the shock-wave–boundary-layer interaction region. The length scales and constants of the forcing function were set as $x_r = 0.5\delta_0$, $z_r = \delta_0$, $a = 0.45$, $b = 0.6$, $c = 0.3$, and $d = 7$. Two values of the forcing amplitude were selected, $A' = A/(\delta_0\rho_{\infty}U_{\infty}^2) = 0.05$ and $A' = 0.025$. These induced appreciable flow perturbations without significant change to the mean-flow structure.

To assess the response of the blunt fin-induced shock-wave–boundary-layer interaction to forcing at different frequencies, two values of the forcing frequency were selected: a low-frequency value $f_0 = 1.22$ kHz ($St_{D,0} = f_0 D/U_{\infty} = 0.0268$) and a midfrequency value $f_0 = 12.2$ kHz ($St_{D,0} = 0.268$). The smaller value of f_0 corresponds to the characteristic low-frequency unsteadiness of the baseline case [observed from the wall-pressure spectra at the 50% shock intermittency (γ) position; see Fig. 4]. The larger value of f_0 (an order of magnitude larger) lies within the range of midfrequency unsteadiness associated with the dynamics of the separation bubble and shear-layer instability [45].

C. Statistical analysis

Following the procedure reported in Ref. [8], the separation shock foot position (X_s) was determined by identifying the location of wall-pressure rise along the centerline of the bottom wall ($y = 0$ and $z = 0$). Here, the pressure threshold was chosen to be higher than the fluctuations that resulted from the upstream forcing. The shock foot velocity (U_s) was subsequently calculated through a central-difference numerical time derivative from the shock position data.

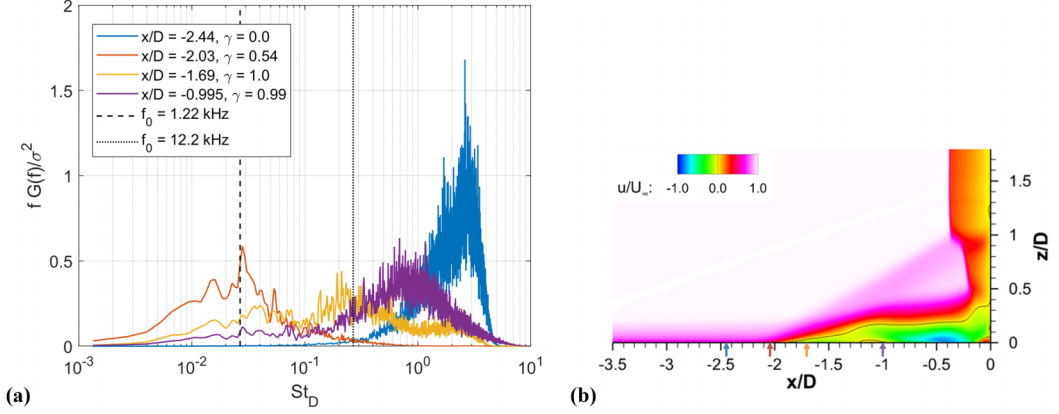


FIG. 4. Baseline case (without forcing): (a) wall-pressure spectra, (b) centerline plane ($y = 0$) mean stream-wise velocity (black outline indicates $u = 0$; arrows indicate positions corresponding to the wall-pressure spectra data).

Fourier analysis of the incoming boundary-layer flow velocity and shock motion fluctuations was performed by calculating the power spectral density estimates $G(f)$ of the respective quantities through Welch's method [54]. The time-history data were segmented into 24 sections of at least 24 300 points, with 50% overlap and Hamming windowing [54].

Low-pass, band-pass, and high-pass Butterworth filters were applied to the shock position data to observe the effects of forcing on the low, mid, and high frequency characteristics of shock motion. The shock velocity data were obtained as numerical time derivatives of the filtered position data. The cutoff frequencies corresponded to $St_D = 0.1$ and $St_D = 1.0$ (see Fig. 5). Hereafter, the subscripts low, mid, and high are used to denote the shock position or velocity data, filtered in the respective ranges.

Phase averages of the shock position and velocity were calculated to assess the relationship between the imposed force and shock motion. The phase was defined based on the input forcing frequency as $\phi = 2\pi f_0 t$, where the phase was constrained to $0 \leq \phi < 2\pi$ using the modulo

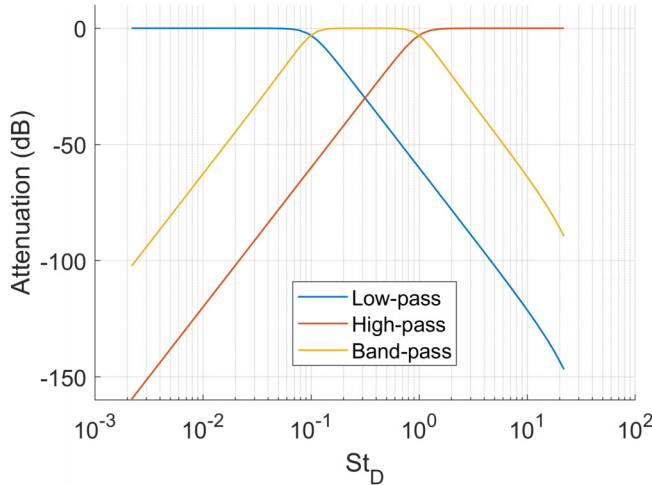


FIG. 5. Filter design.

TABLE II. Cases considered in the present work.

Case	Forcing frequency		Forcing amplitude A'
	f_0 (kHz)	$St_{D,0}$	
0		Baseline flow, Ref. [8]	
1	1.22	0.0268	0.05
2	12.2	0.268	0.05
3	1.22	0.0268	0.025
4	12.2	0.268	0.025

operation (remainder). For the baseline (without forcing) case, the phase was calculated using $f_0 = 1.22$ kHz, which corresponds to the characteristic low-frequency shock unsteadiness.

Cross correlations between the time-periodic force [represented as $\cos(2\pi f_0 t)$] and shock motion time series were also analyzed. The correlation coefficients were normalized using the standard deviation of the input data, such that the autocorrelations at zero lag were unity.

III. RESULTS

The results of the baseline case (without forcing) were reported in our previous study, Ref. [8]. In that study, we found fairly good agreement between the predictions of the detached eddy simulations and experimental measurements. In the present work, a parametric study with upstream forcing at two frequencies and two forcing amplitudes was performed. The various cases are summarized in Table II.

It is computationally costly to carry out calculations that resolve the low-frequency content in this class of flows. To achieve statistical convergence of the low-frequency content, each case was run for at least 300 000 time steps, which is equivalent to approximately 92 cycles of the characteristic low-frequency shock motion ($f = 1.22$ kHz or $St_D = 0.0268$). Data along the centerline ($y = 0$) plane were saved at every time step (equivalent to a sampling frequency of 4 MHz).

To give an overview of the flow structure, the instantaneous flow field of the baseline case (case 0) is shown in Fig. 6. The vortical structures are visualized through an isosurface of Q criterion, colored by the streamwise velocity. The shock structure is indicated by gray isocontours of the density gradient magnitude. In this image, only half of the domain ($y > 0$) is shown for clarity. Defining features of the blunt fin-induced shock-wave–boundary-layer interaction such as the separation shock, reattachment shock, inviscid shock, and separated flow region are clearly visible. For all cases, disturbances are introduced at the inlet plane through the synthetically generated

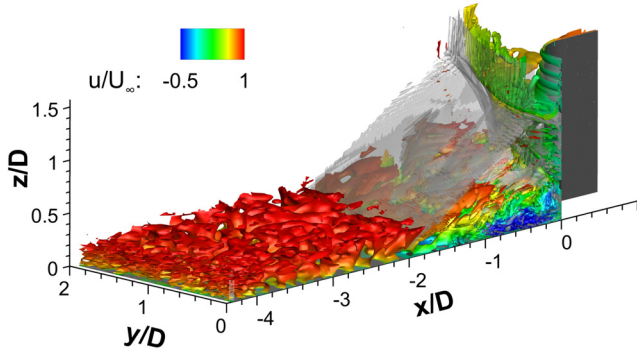


FIG. 6. Instantaneous flow field (baseline case).

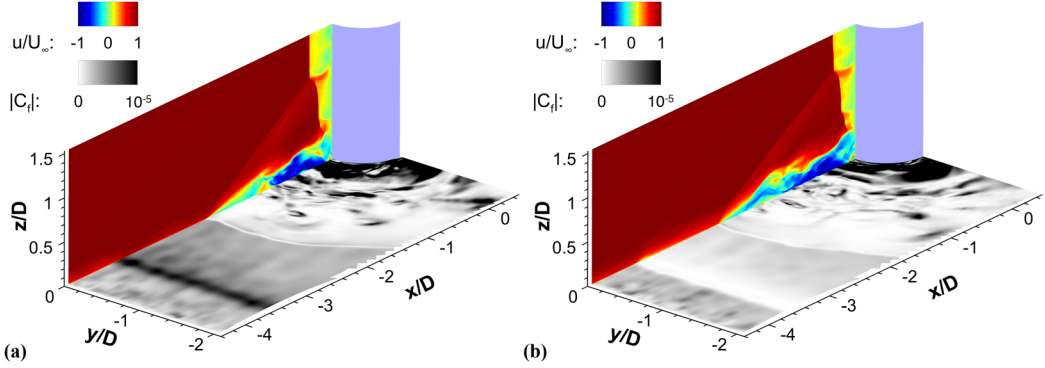


FIG. 7. Instances with upstream forcing (case 1): (a) maximum downstream acting force ($\phi = 0$), (b) maximum upstream acting force ($\phi = \pi$).

turbulence. Due to the grid resolution and eddy viscosity in the RANS part of the calculations, small-scale turbulence dissipates in the incoming boundary layer. Large-scale structures on the order of the boundary-layer thickness enter the interaction region. Small-scale unsteady structures can be observed within the separation region (between the separation shock and the fin leading edge), generated by instability of the separated shear layer.

The local effects of upstream forcing are demonstrated in Fig. 7. Here, two instances representing the maximum downstream acting force and maximum upstream acting force were chosen from the low-frequency, large-amplitude forcing case (case 1). The influence of forcing on the near-wall streamwise velocity and skin-friction magnitude on the bottom wall can be clearly observed. When the force acts upstream, a weak Mach wave is induced near the source origin ($x_1/D = -3.5$) due to the thickening of the boundary layer.

Since changes in the RANS–LES transition location could be mistaken for changes in the flow physics, it is necessary to show that this location does not substantially change when flow control is applied. This issue is addressed in Figs. 8 and 9, which, respectively, show the mean and instantaneous RANS–LES transition boundary.

For the baseline case (case 0), the calculation started to transition from RANS to LES immediately downstream of the separation shock [see Fig. 9(a)]. To investigate the effect of upstream forcing on the RANS–LES transition behavior, the mean transition line along the centerline plane was extracted and is shown for all five cases in Fig. 8. As illustrated in this figure, the region between the bottom wall ($z = 0$) and the isolines (corresponding to the various cases) was solved using RANS modeling. Moving away from the isolines in the positive wall-normal direction, the modeled turbulent viscosity decreases, and the calculations start to transition into LES. In the mean data, the RANS–LES transition occurs upstream of the mean separation shock foot (see Fig. 8). The situation is different, however, in the instantaneous flow. Samples of the instantaneous transition line in Fig. 9 show that the instantaneous RANS–LES transition boundary is adjacent to the separation shock foot.

Some effect of upstream forcing on the mean RANS–LES transition behavior was observed. With upstream forcing, partial transition occurred slightly upstream of the source origin ($x_1/D = -3.5$). The effect was stronger for the cases with larger forcing amplitude (cases 1 and 2). As the perturbations convect and dissipate downstream, the RANS–LES transition boundary moves away from the wall, approaching the location seen in the baseline case (case 0). Farther downstream ($-2.7 < x/D < -2.3$), the flow unsteadiness and separation within the interaction region caused the onset of complete transition to LES. In this region, the earlier onset of transition with upstream forcing is a consequence of the larger upstream influence and more upstream position of the separation shock foot (see Fig. 13). Since the ultimate objective of superposing perturbations of

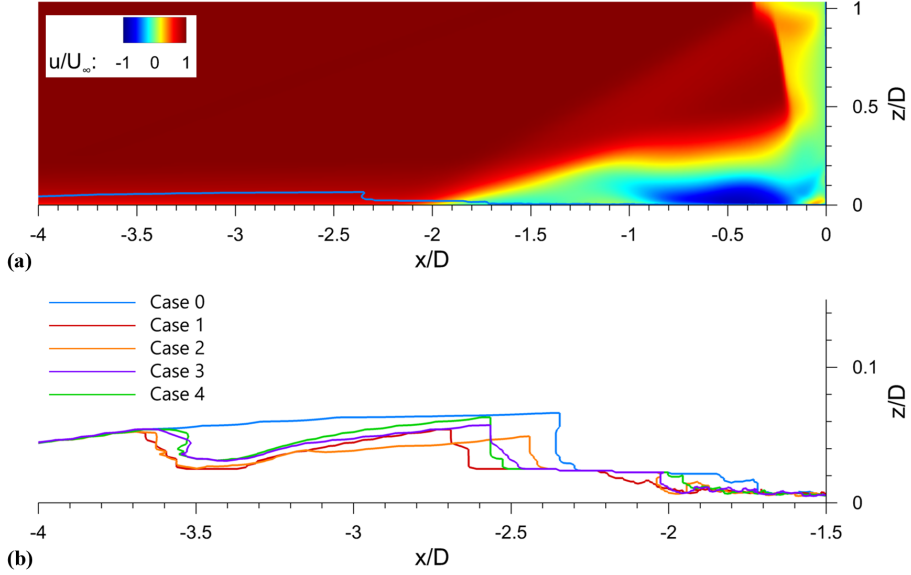


FIG. 8. Mean RANS-LES transition along centerline ($y=0$) plane: (a) baseline case (case 0) with background contour of mean streamwise velocity, (b) effect of upstream forcing (magnified field of view). Isolines denote the boundary of the RANS-dominated region.

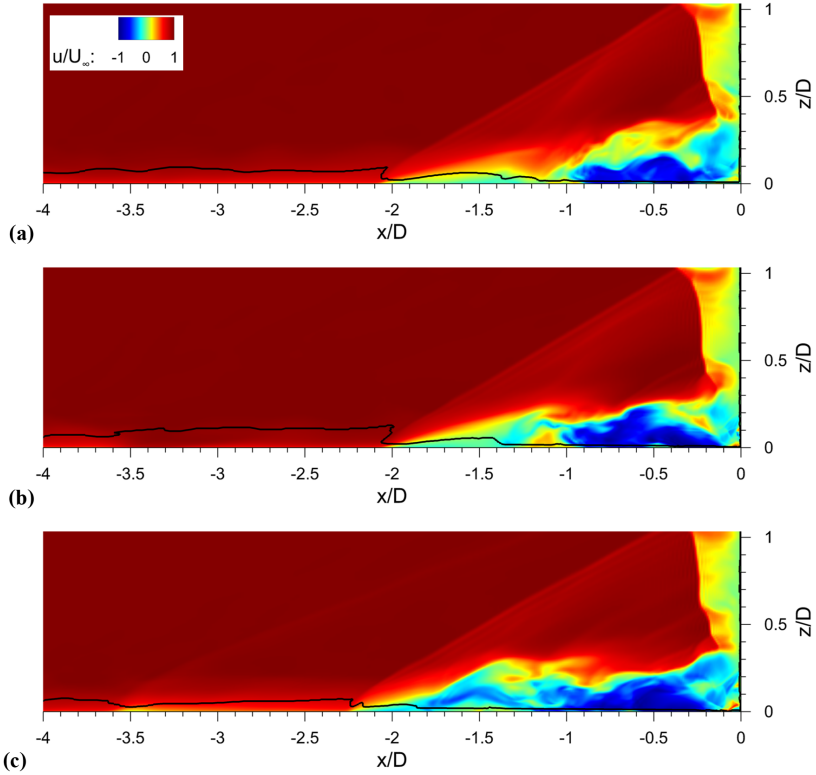


FIG. 9. Instantaneous RANS-LES transition along centerline ($y=0$) plane: (a) case 0, (b) case 1 at $\phi = 0$, (c) case 1 at $\phi = \pi$. Black isolines denote the boundary of the RANS-dominated region.

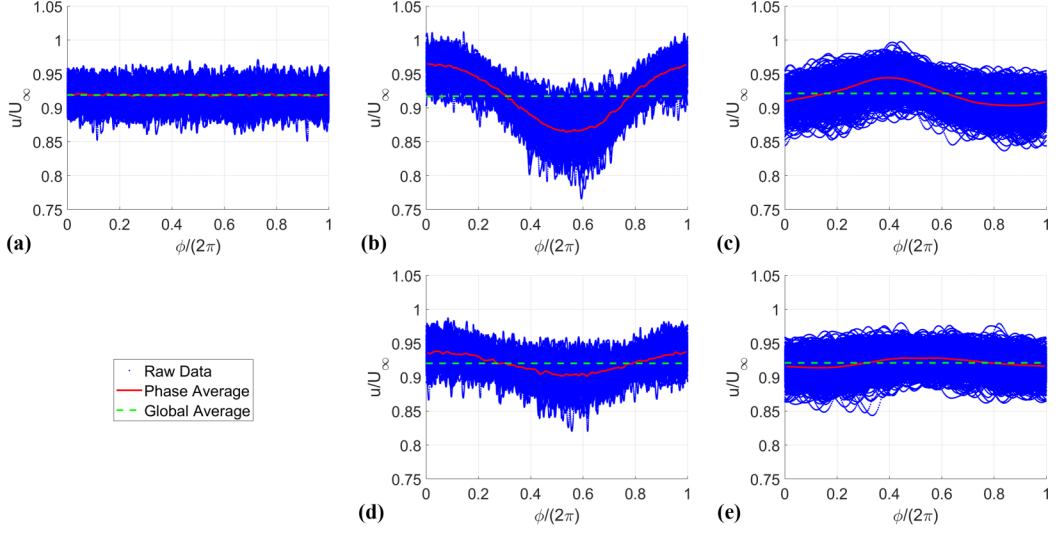


FIG. 10. Phase average of incoming boundary-layer streamwise velocity at $z/\delta_0 = 0.5$: (a) case 0, (b) case 1, (c) case 2, (d) case 3, (e) case 4.

a specific form onto the incoming flow to the interaction region was achieved (see the following section), these small differences in RANS–LES transition due to upstream forcing were deemed to be acceptable.

A. Effect on incoming flow

A time-dependent velocity profile of the incoming boundary-layer flow was extracted at a location downstream of the forcing origin, and upstream of the shock-wave–boundary-layer interaction region. For the baseline case (case 0), the upstream location was $x/D = -2.44$. With forcing (cases 1 to 4), due to the slightly larger separation length, the upstream location was set as $x/D = -2.70$.

The phase-averaged streamwise velocity at the midpoint of the boundary layer height ($z/\delta_0 = 0.5$) is shown in Fig. 10 for the five cases. The global time-averaged data and the raw data are also shown for reference. As expected for the baseline case (case 0), the phase average is identical to the global average. With low-frequency forcing (cases 1 and 3), the incoming boundary-layer flow exhibited a sinusoidal fluctuating component that is consistent with the input forcing function. With midfrequency forcing (Cases 2 and 4), the perturbations in streamwise velocity were comparatively smaller in magnitude, but nonetheless present. The amplitudes of these perturbations scaled with the chosen values of the forcing amplitude.

Figure 11 shows that the wall-normal profile of the phase-averaged velocity perturbations was qualitatively similar to the desired profile (compare to Fig. 3). The magnitude of the velocity perturbations is seen to increase with the amplitude of the forcing, and to decrease as the forcing frequency is moved away from the characteristic low-frequency scale.

Power spectra of the streamwise flow velocity fluctuations are plotted in the premultiplied form with and without normalization in Fig. 12. With forcing (cases 1 to 4), features corresponding to the input forcing frequencies and the respective second harmonics can be observed. The unnormalized data show that the application of upstream forcing across the various combinations of forcing frequencies and amplitudes did not affect the unsteadiness of the incoming flow at higher frequencies ($St_D \sim 1$).

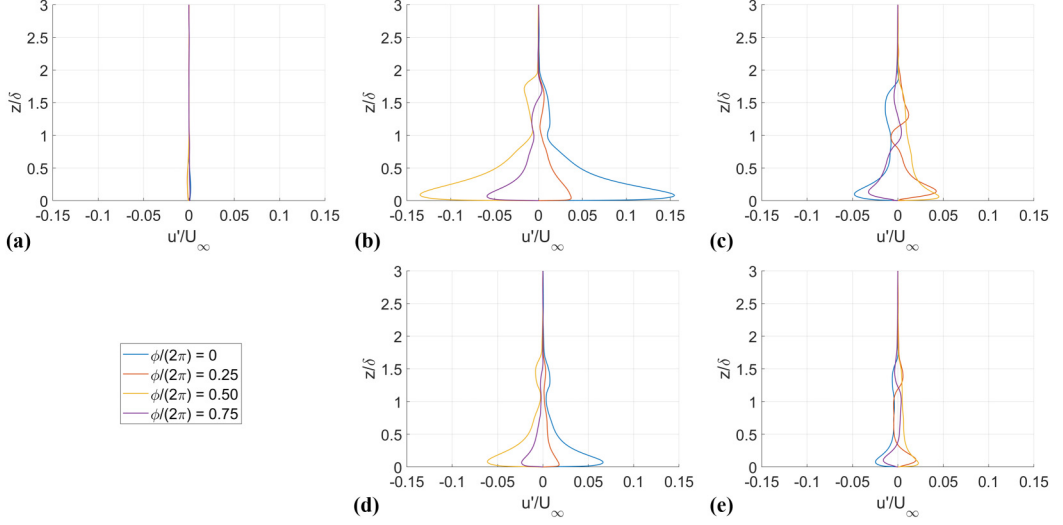


FIG. 11. Phase-averaged incoming boundary-layer streamwise velocity perturbation profile: (a) case 0, (b) case 1, (c) case 2, (d) case 3, (e) case 4.

B. Effect on mean-flow characteristics

The aim of the forcing was to introduce an unsteady perturbation in the incoming flow with a relatively small effect on the mean-flow characteristics. An initial check of the magnitude of the effect of forcing was carried out by examining the pressure and skin friction on the wall ahead of the fin.

The mean and root-mean-square (rms) fluctuations of the wall pressure and streamwise skin-friction coefficient along the plate centerline ($y = 0$ and $z = 0$) for the different cases are shown in Fig. 13. The upstream influence length of the shock-wave–boundary-layer interaction increased slightly with forcing. Defining the separation length (L_{sep}) as the distance from the fin leading edge

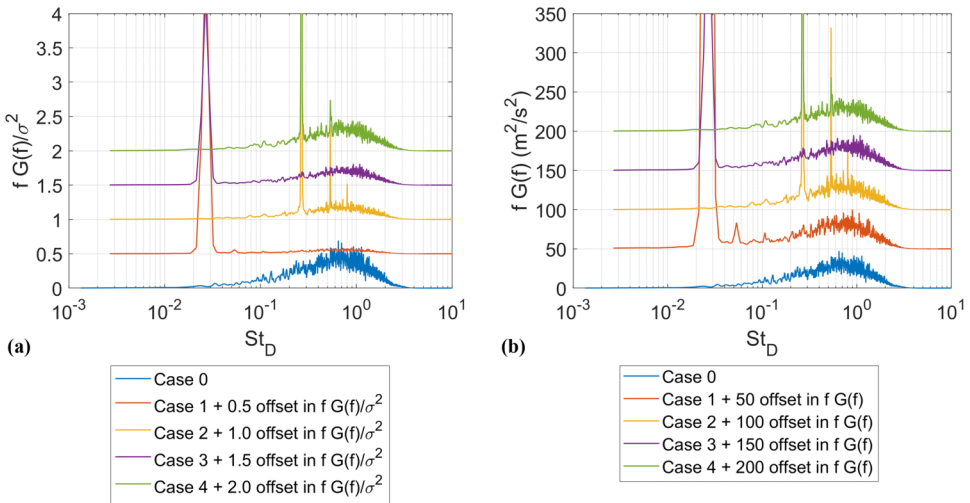


FIG. 12. Incoming boundary-layer streamwise velocity spectra at $z/\delta_0 = 0.5$: (a) with normalization, (b) without normalization.

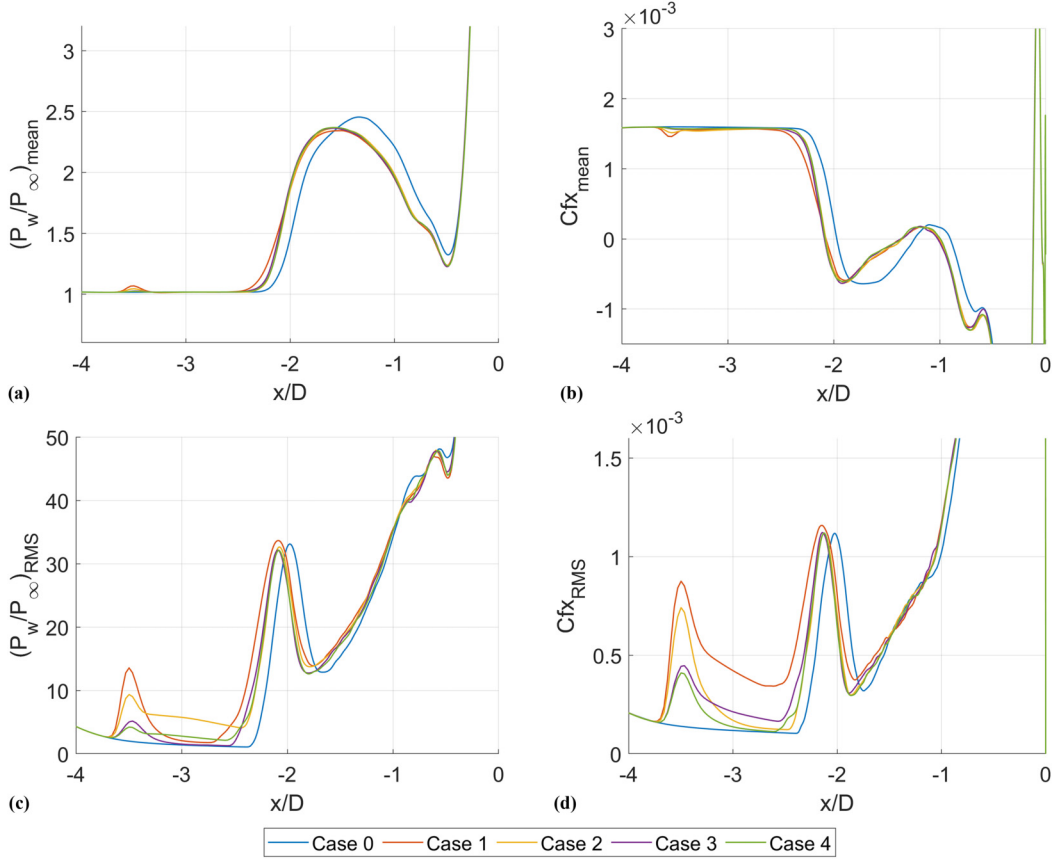


FIG. 13. Plate centerline wall pressure and streamwise skin-friction coefficient: (a), (b) mean, (c), (d) rms.

to the primary separation line (first instance of $C_{fx} = 0$ after the separation shock), $L_{\text{sep}}/D = 1.97$ for the baseline case (case 0). For all of the cases with forcing (cases 1 to 4), $L_{\text{sep}}/D = 2.07$. The maximum pressure ($P_{w,\text{max}}$) within the separation region (around $x/D = -1.5$) decreased slightly. For the baseline case, $P_{w,\text{max}}/P_\infty = 2.46$. With forcing, $P_{w,\text{max}}/P_\infty$ ranged from 2.34 to 2.37.

The perturbation in the rms fluctuations from the applied unsteady force can be clearly seen around the source origin ($x_1/D = -3.5$). The peak values of these perturbations increased non-linearly with the input forcing amplitude. The rms fluctuations of the pressure and skin friction decayed at varying rates with downstream distance from the source origin. With low-frequency forcing (cases 1 and 3), the rms pressure fluctuations decreased rapidly to baseline values, while the rms skin-friction coefficient fluctuations decayed more gradually. The opposite was observed with midfrequency forcing (cases 2 and 4), where the rms pressure fluctuations decreased at a slower rate compared to that of the skin-friction coefficient. The peak values of the rms fluctuations in pressure and skin-friction coefficient around the mean separation shock foot ($X_s/D \approx -2$) did not change significantly with forcing.

Inspection of the mean and rms quantities of the flow-field parameters along the centerline plane ($y = 0$) also revealed no significant change due to upstream forcing. For example, Fig. 14 shows the mean and rms fluctuations of the density between the baseline case (case 0) and cases with larger forcing amplitude (cases 1 and 2). Other than the relatively weak Mach wave induced around the forcing origin, and minor changes in the magnitude of the rms fluctuations associated with the

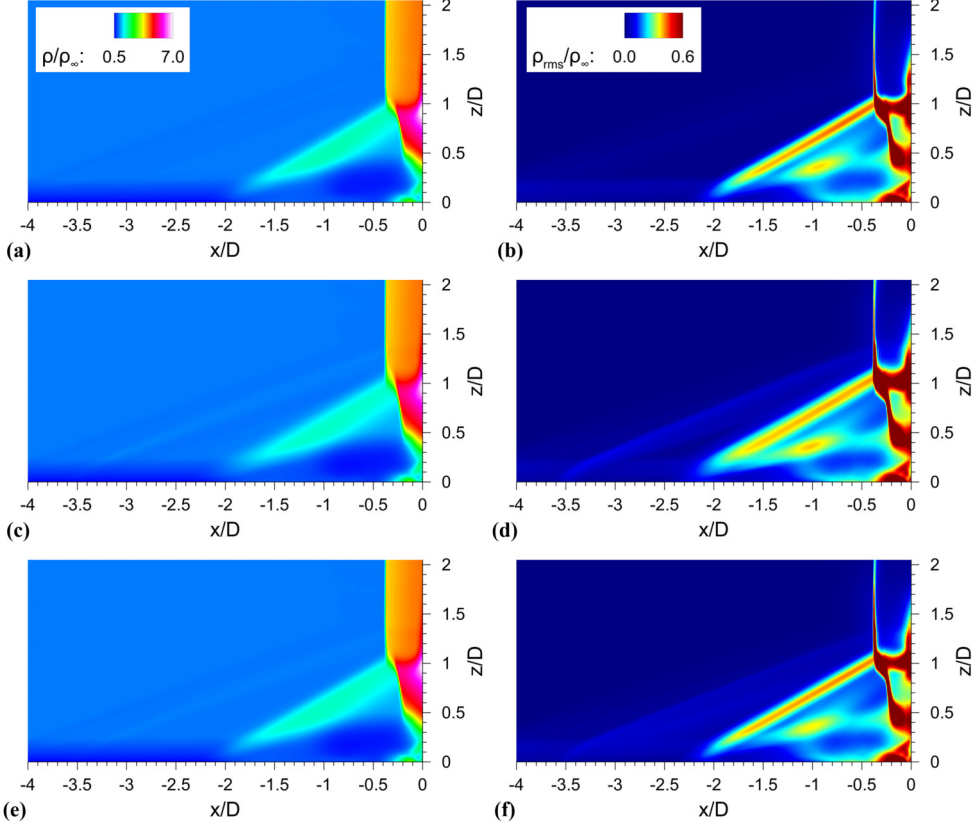


FIG. 14. Centerline ($y = 0$) plane mean (left) and rms (right) density: (a), (b) case 0, (c), (d) case 1, (e), (f) case 2.

separation shock and separated shear layer, there was no substantial difference in the mean-flow characteristics.

In summary, while some effects of the applied force may be observed, the change in the mean-flow features around the shock-wave-boundary-layer interaction region was not significant. These results are consistent with the desired effect of the forcing, which was to alter the separation motion without significantly changing the mean flow.

C. Effect on shock motion

Despite the small effect of forcing on the mean flow, significant effects of forcing on the instantaneous separation shock motion were observed. Figure 15 shows the phase-averaged shock position for each case. In the absence of forcing, case 0 shown in Fig. 15(a), the phase average is a constant profile. This result is expected; the uncorrelated motion for the baseline case disappears under phase averaging. For forcing at the characteristic low-frequency value, cases 1 and 3 shown in Fig. 15(b) and Fig. 15(d), a distinct sinusoidal pattern appears in the average shock position profile. For the higher-frequency forcing, cases 2 and 4 shown in Fig. 15(c) and Fig. 15(e), a sinusoidal pattern also appears, but its amplitude is significantly lower.

To examine the shock motion in different frequency bands (low, mid, and high), the shock foot position data were digitally filtered (see Fig. 5), and the associated shock foot velocity data were computed. The phase averages of these data are shown in Figs. 16–19. The peak-to-peak amplitude

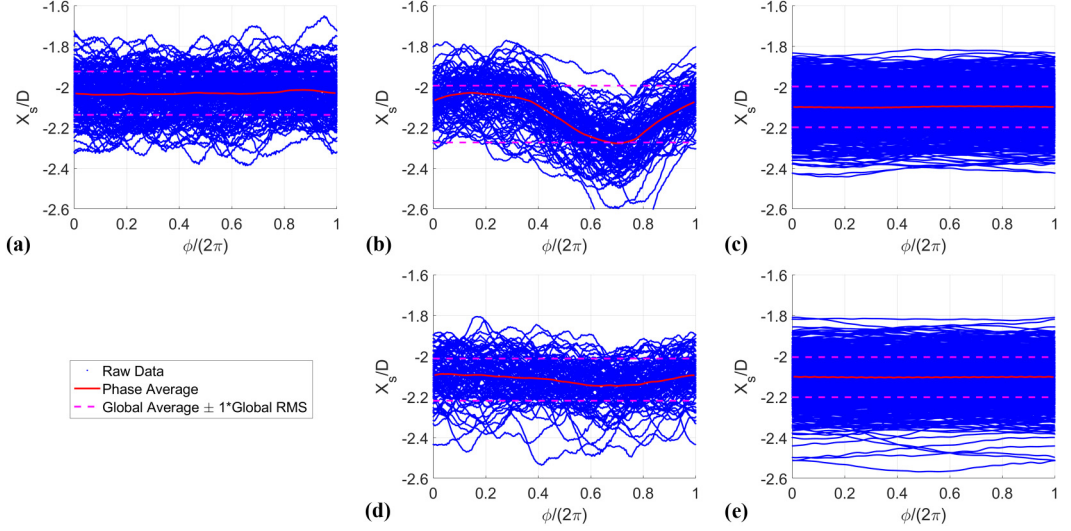


FIG. 15. Phase-averaged shock position: (a) case 0, (b) case 1, (c) case 2, (d) case 3, (e) case 4.

of the phase averaged shock position and velocity normalized against the respective global rms fluctuation values for the different cases are shown in Table III.

In general, similar observations may be made from the shock position (Fig. 15) and low-pass filtered shock velocity data (Fig. 16). In the phase averaged band-pass filtered shock velocity (Fig. 17), the baseline case and low-frequency forcing cases show random perturbations that would likely diminish to zero on averaging with more data. With midfrequency forcing, a sinusoidal-like profile was obtained (see Fig. 19 for clarity). However, its amplitude was relatively small compared to the global rms fluctuations of this frequency band. In the high-pass filtered shock velocity data (Fig. 18), the phase averages for all five cases are essentially constant.

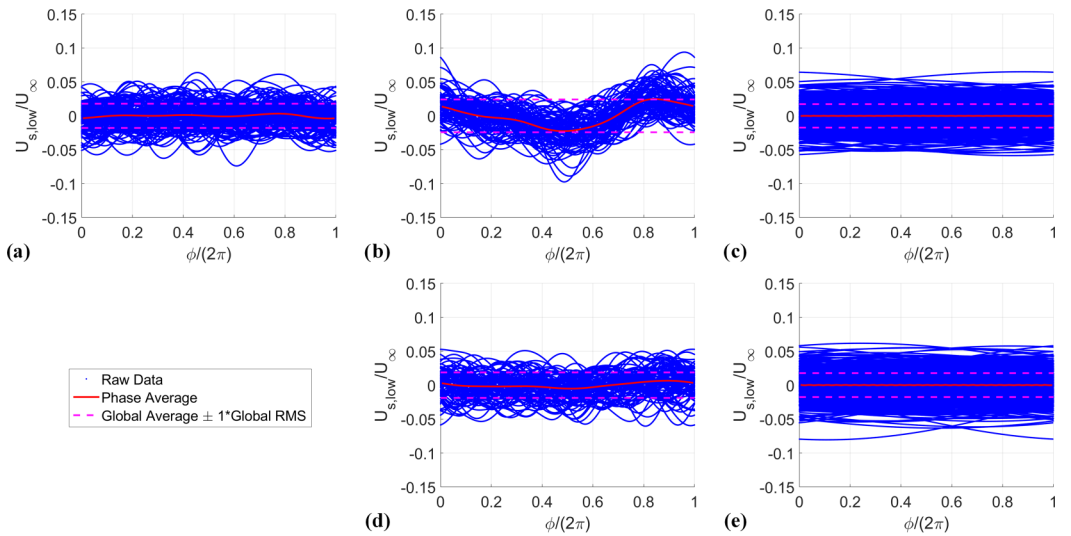


FIG. 16. Phase-averaged low-pass filtered shock velocity: (a) case 0, (b) case 1, (c) case 2, (d) case 3, (e) case 4.

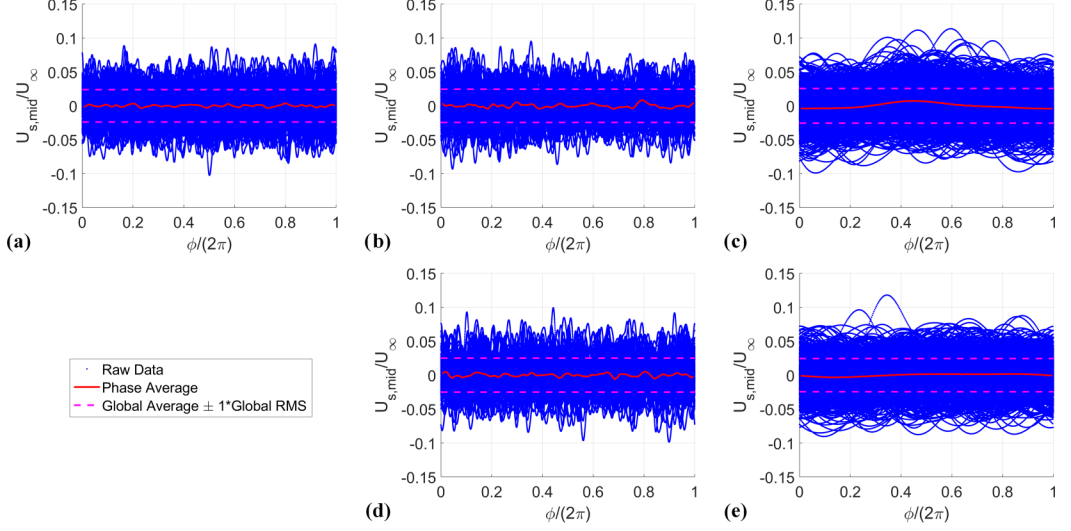


FIG. 17. Phase-averaged band-pass filtered shock velocity: (a) case 0, (b) case 1, (c) case 2, (d) case 3, (e) case 4.

An analysis, corresponding to that of the shock foot position (X_s) and velocity (U_s), was performed on the flow separation location (X_{sp}) and associated velocity (U_{sp}), where the separation location was defined as the first instance of $C_{fx} = 0$ downstream of the separation shock. The phase-averaged motion of the separation location is compared with that of the shock motion in Fig. 20. With midfrequency forcing, some phase difference is observed in the band-pass filtered velocities [see Fig. 20(d)], but the primary effects of forcing on the shock motion could also be observed in the separation motion. These separation location statistics demonstrate that the

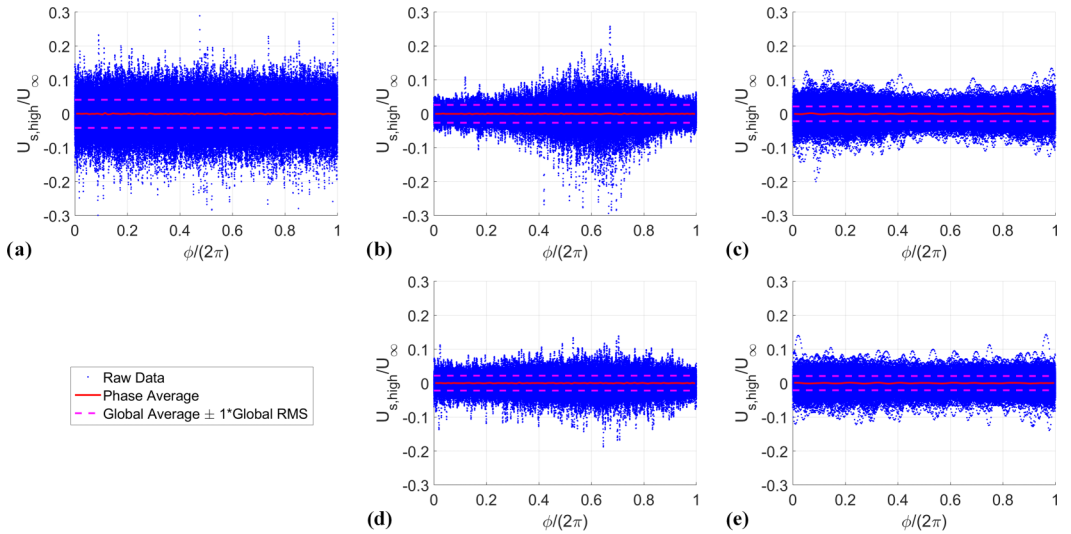


FIG. 18. Phase-averaged high-pass filtered shock velocity: (a) case 0, (b) case 1, (c) case 2, (d) case 3, (e) case 4.

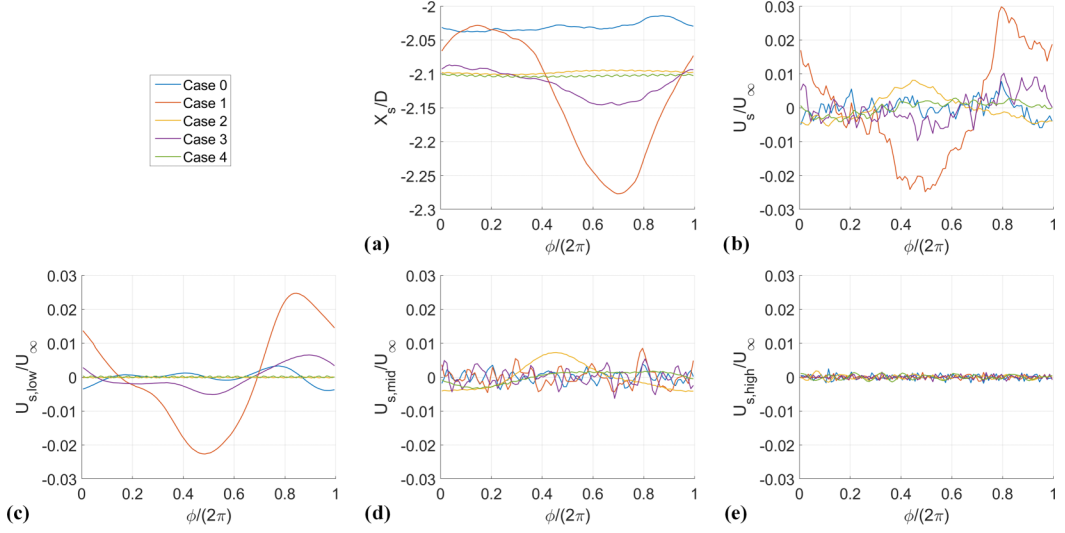


FIG. 19. Effect of forcing on phase-averaged shock motion: (a) shock position, (b) unfiltered shock velocity, (c) low-pass filtered shock velocity, (d) band-pass filtered shock velocity, (e) high-pass filtered shock velocity.

shock location determined by the instantaneous wall pressure rise is an effective surrogate for the separation location.

These observations of the phase averages indicate that the shock-wave–boundary-layer interaction was responsive to the imposed upstream forcing, and that the motion of the instantaneous separation location and separation shock were phase locked with the input signal. The results were dependent on the frequency of forcing. With a forcing frequency representative of the characteristic large-scale separation unsteadiness in the baseline flow, a strong response was observed. The separation region did not, however, respond strongly to disturbances in a higher frequency range. A larger forcing amplitude led to greater separation motion, with a nonlinear increase in separation motion. The separation motion of the self-oscillating blunt fin flow is seen to be selectively modulated by upstream forcing.

To corroborate these conclusions, cross correlations between the shock perturbations and time-periodic force are shown in Fig. 21. This analysis refines the earlier examination of the phase-averaged parameters to ascertain the response of the separation shock motion to the imposed forcing. With low-frequency forcing (cases 1 and 3), significant correlation ($\rho > 0.2$) between the shock position perturbations and input force was obtained. The strength of the correlation scaled with the input forcing amplitude. Looking at Fig. 22, with the larger forcing amplitude $A' = 0.05$, the maximum value of the correlation coefficient was 0.62 and it decreased to 0.2 over a time lag of about 59 forcing cycles (in both positive and negative lag directions). With the smaller forcing

TABLE III. Peak-to-peak amplitude of phase-averaged separation shock foot position and velocity parameters (normalized against the respective global rms fluctuation values).

Parameter	Case 0	Case 1	Case 2	Case 3	Case 4
X_s/D	0.22	1.78	0.08	0.57	0.06
U_s/U_∞	0.26	1.22	0.34	0.50	0.18
$U_{s,low}/U_\infty$	0.41	1.96	0.03	0.62	0.04
$U_{s,mid}/U_\infty$	0.32	0.53	0.45	0.46	0.21
$U_{s,high}/U_\infty$	0.10	0.10	0.15	0.13	0.13

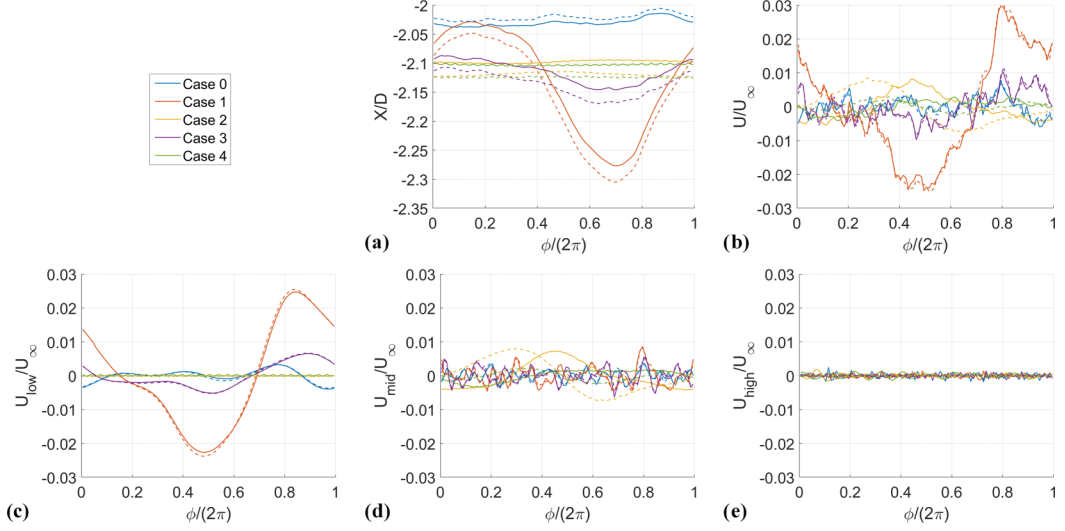


FIG. 20. Effect of forcing on phase-averaged shock (continuous lines) and separation motion (broken lines): (a) position, (b) unfiltered velocity, (c) low-pass filtered velocity, (d) band-pass filtered velocity, (e) high-pass filtered velocity.

amplitude $A' = 0.025$, the maximum value of the correlation coefficient was 0.24 and it decreased to 0.2 over a time lag of about 16 forcing cycles. Significant correlation was also observed between the low-pass filtered shock velocity perturbations and input force. With midfrequency forcing (cases 2 and 4), no significant correlation with the input force was found across the various shock position and velocity parameters. Looking at the cross correlation between the band-pass filtered shock velocity perturbations and input force term, the magnitude of the correlation coefficient was

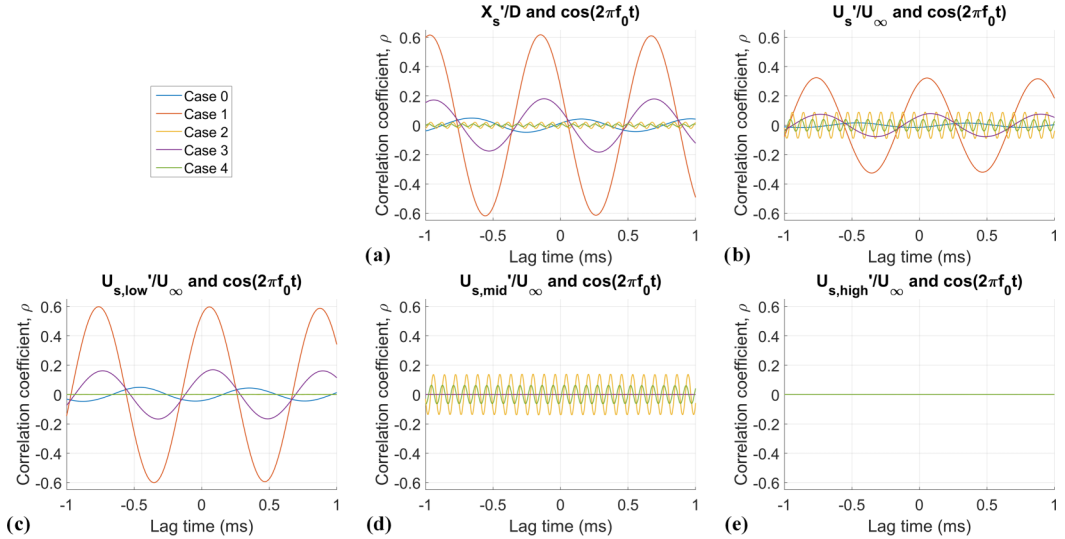


FIG. 21. Cross correlations between imposed force and shock motion: (a) shock position, (b) unfiltered shock velocity, (c) low-pass filtered shock velocity, (d) band-pass filtered shock velocity, (e) high-pass filtered shock velocity.

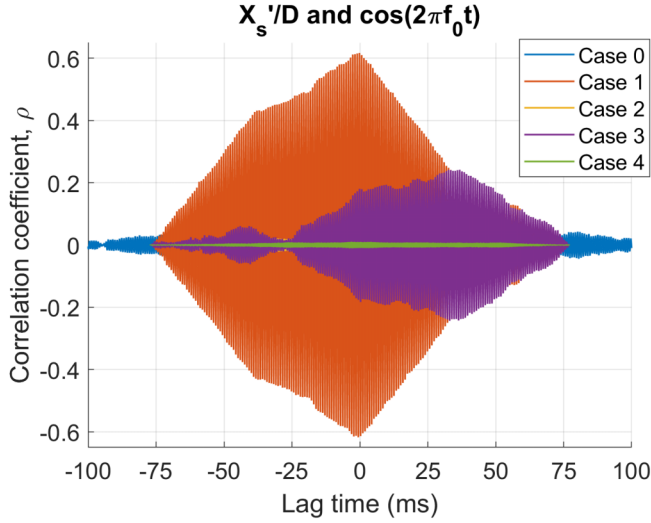


FIG. 22. Cross correlations between imposed force and shock position (larger timescale).

two orders of magnitude larger than that of the baseline case and low-frequency forcing cases. Analysis of the cross correlations supports the earlier observations; with low-frequency forcing, the separation shock motion was phase-locked to the input upstream force. The correlation with mid-frequency forcing was small.

The rms fluctuations of the shock position and velocity data (calculated with reference to the global average of the respective parameters) are shown in Table IV. Comparison of these parameters shows the effect of upstream forcing on the degree of unsteadiness in the shock motion. With low-frequency forcing (cases 1 and 3), compared to the baseline case (case 0), the rms of the shock position and low-pass filtered shock velocity fluctuations increased, reflecting the expected influence from the input perturbations, particularly for the case with larger forcing amplitude (case 1). Although the case with smaller forcing amplitude (case 3) did not show appreciable increase in these parameters, the strong response of the flow to its low-frequency forcing is nonetheless evident in the phase-averaged parameters shown earlier in Fig. 19. For both small and large forcing amplitudes, the rms of the band-pass filtered shock velocity fluctuations remains unchanged, while that of the high-pass filtered shock velocity fluctuations decreased. With midfrequency forcing (cases 2 and 4), there was minimal change in the rms fluctuations of the shock position, low-pass filtered shock velocity, and band-pass filtered shock velocity compared to the baseline case. A large reduction in the rms value of the high-pass filtered shock velocity fluctuations was also observed for the midfrequency forcing cases.

For all cases with upstream forcing, the rms value of the unfiltered shock velocity fluctuations decreased from the baseline value. Comparison of the rms values corresponding to the low-pass,

TABLE IV. rms of shock position and velocity fluctuations.

Parameter	Case 0	Case 1	Case 2	Case 3	Case 4
X_s/D	0.107	0.140	0.100	0.104	0.099
U_s/U_∞	0.052	0.045	0.039	0.040	0.038
$U_{s,low}/U_\infty$	0.018	0.024	0.017	0.019	0.018
$U_{s,mid}/U_\infty$	0.024	0.025	0.026	0.025	0.024
$U_{s,high}/U_\infty$	0.041	0.026	0.022	0.022	0.021

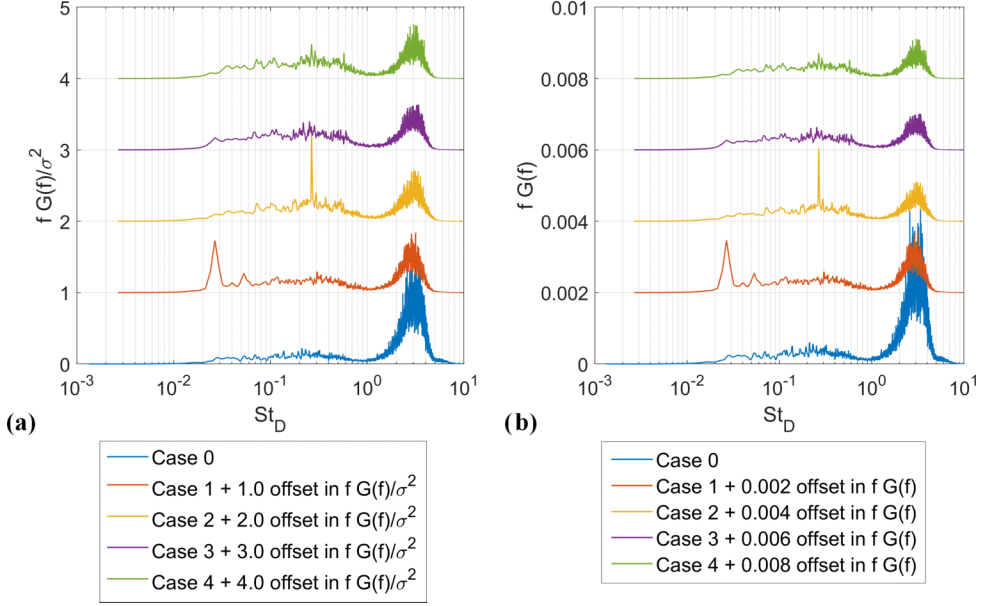


FIG. 23. Shock velocity spectra: (a) with normalization, (b) without normalization.

band-pass, and high-pass filtered shock velocity fluctuations shows a significant difference in the proportion of unsteadiness across the frequency bands. For the baseline case (case 0), the unsteadiness in the shock velocity appears to be concentrated in the higher frequencies. With upstream forcing (cases 1 to 4), the unsteadiness in the shock velocity appears to be more evenly distributed between the frequency bands, though some bias to the midfrequencies is observed.

The decrease in high-pass filtered shock velocity perturbations in the cases with upstream forcing (relative to the baseline case), which can also be observed in the high-pass filtered shock velocity phase history in Fig. 18, was unexpected. Furthermore, the un-normalized spectra of the unfiltered shock velocity (see Fig. 23) show a reduction in spectral energy around the high-frequency range ($St_D > 1$) for the cases with upstream forcing (cases 1 to 4). While more investigation is required to understand the reason for the reduction in high-frequency unsteadiness of the separation shock motion with upstream forcing, some useful observations may be made from the present data. As discussed earlier, the upstream forcing in these calculations did not affect the degree of high-frequency unsteadiness in the streamwise velocity fluctuations extracted upstream of the interaction region (see Fig. 12). In other words, the upstream forcing did not attenuate the high-frequency turbulent fluctuations of the flow entering the interaction region, which could have otherwise led to the muted high-frequency unsteadiness of the separation shock motion. This reduction in high-frequency unsteadiness of the separation shock motion could possibly be a response of the shock-wave–boundary-layer interaction to the input force itself.

IV. SUMMARY AND CONCLUSIONS

Detached eddy simulations of a Mach 3, turbulent flow over a blunt fin were performed. This configuration is known to generate a large, three-dimensional, unsteady, separated region, and such strong streamline curvature is thought to influence the nature of the flow unsteadiness [43]. Our previously published detached eddy simulations [8] exhibited large-scale unsteadiness even in the absence of fluctuations in the incoming flow. In that study, the introduction of synthetic turbulence at the inflow boundary was found to alter the separation motion.

Some authors [45,55] have reported that separation motion is insensitive to external forcing, but other studies, in both subsonic and supersonic flow [7,33,42], have found a response in the separation zone to upstream disturbances. In the responsive flows, the upstream disturbances seem to be required to maintain the separation oscillations. In contrast, the blunt fin flow exhibits self-excited oscillations, and the modulation of these oscillations by upstream disturbances is of interest for flow control applications.

To explore the effects of upstream disturbances on the blunt fin flow, a parametric study was carried out of the response of the flow to time-periodic forcing of the incoming boundary layer. The disturbances were introduced into the boundary layer through momentum and energy source terms.

Following the procedure of Ref. [7], the spatial form of the source terms was based on averages of the baseline flow, conditioned on the motion of the separation shock. The profile of the applied force was uniform in the spanwise direction and exponentially decreasing in the streamwise direction from the origin of the source. The wall-normal profile was based on conditional averages of the incoming boundary-layer streamwise velocity profile. The temporal variation of the force was sinusoidal, and two forcing frequencies were tested: a low-frequency $f_0 = 1.22$ kHz ($St_{D,0} = 0.0268$), representative of the large-scale separation motion in the baseline flow, and a midfrequency $f_0 = 12.2$ kHz ($St_{D,0} = 0.268$), representative of perturbation by structures on the scale of the local shear-layer thickness. Two values of the forcing amplitude were evaluated: $A' = 0.05$ and $A' = 0.025$.

With future flow control applications in mind, an aim of this study was to introduce a small, unsteady perturbation in the incoming flow with a relatively small effect on the mean-flow characteristics. This end was achieved; there was no significant change in the mean and root-mean-square statistics of wall pressure and skin friction in regions of the flow away from the immediate vicinity of the forcing.

The separation motion, however, did respond to the perturbations in the incoming flow. The root-mean-square fluctuations of the shock position and shock velocity increased with forcing, and the corresponding spectra displayed peaks corresponding to that of the applied force. Unexpectedly, the high-frequency ($St_D > 1$) unsteadiness of the shock motion appeared to be reduced in the cases with upstream forcing.

The response of the separation shock motion to the imposed perturbations was found to be dependent on the frequency of forcing. With a forcing frequency representative of the characteristic large-scale separation unsteadiness in the baseline flow, phase averages of shock position and velocity indicated that the separation shock motion was phase locked to the applied force, and a larger forcing amplitude led to greater separation motion. The separation region did not, however, respond strongly to disturbances in a higher frequency range.

The present results show that in a flow that oscillates in the absence of upstream disturbances, separation motion can be modulated by upstream forcing of a particular form. Similar results have been obtained in the past for flows where separation unsteadiness is directly driven by incoming turbulence, but the modulation of self-excited oscillations in the present class of flow is a different behavior. It suggests opportunities for flow control of strong shock-wave–boundary-layer interactions.

ACKNOWLEDGMENT

Computational resources were provided by Purdue University's Rosen Center for Advanced Computing.

[1] N. T. Clemens and V. Narayanaswamy, Low-frequency unsteadiness of shock wave/turbulent boundary layer interactions, *Annu. Rev. Fluid Mech.* **46**, 469 (2014).

- [2] D. R. Chapman, D. M. Kuehn, and H. K. Larson, Investigation of separated flows in supersonic and subsonic streams with emphasis on the effect of transition, NACA Report No. 1356 (1958).
- [3] A. L. Kistler, Fluctuating wall pressure under a separated supersonic flow, *J. Acoust. Soc. Am.* **36**, 543 (1964).
- [4] D. S. Dolling, Fifty years of shock-wave/boundary-layer interaction research: What next? *AIAA J.* **39**, 1517 (2001).
- [5] D. V. Gaitonde, Progress in shock wave/boundary layer interactions, *Prog. Aerosp. Sci.* **72**, 80 (2015).
- [6] K. M. Porter and J. Poggie, Selective upstream influence on the unsteadiness of a separated turbulent compression ramp flow, *Phys. Fluids* **31**, 016104 (2019).
- [7] J. Poggie, Effect of forcing on a supersonic compression ramp flow, *AIAA J.* **57**, 3765 (2019).
- [8] H. Ngoh and J. Poggie, Detached eddy simulation of blunt-fin-induced shock-wave/boundary-layer interaction, *AIAA J.* **60**, 2097 (2022).
- [9] M. C. Galbraith and P. D. Orkwis, *Multi-Row Micro-Ramp Actuators for Shock Wave Boundary-Layer Interaction Control*, AIAA Paper No. 2009-321 (American Institute of Aeronautics and Astronautics, Reston, VA, 2009).
- [10] M. L. Funderburk and V. Narayanaswamy, *Experimental Investigation of Microramp Vortex Generator Application Upstream of an Axisymmetric Shock Boundary Layer Interaction*, AIAA Paper No. 2018-4937 (American Institute of Aeronautics and Astronautics, Reston, VA, 2018).
- [11] M. J. Schwartz, K. M. Stamper, R. B. Bond, and J. D. Schmisser, *Passive Flow Control on Crossing Shock-Wave/Boundary-Layer Interactions*, AIAA Paper No. 2019-3595 (American Institute of Aeronautics and Astronautics, Reston, VA, 2019).
- [12] V. Shinde, J. McNamara, and D. V. Gaitonde, Control of transitional shock wave boundary layer interaction using structurally constrained surface morphing, *Aerosp. Sci. Technol.* **96**, 105545 (2020).
- [13] S. Lee and A. Gross, *Numerical Investigation of Effect of Corrugated Wall on Supersonic Turbulent Shock-Wave Boundary Layer Interaction*, AIAA Paper No. 2021-2765 (American Institute of Aeronautics and Astronautics, Reston, VA, 2021).
- [14] Y.-L. Lin, M. J. Rimlinger, T. I.-P. Shih, and B. P. Willis, *Control of Shock-Wave/Boundary-Layer Interactions with Passive Blowing and Bleeding*, AIAA Paper No. 97-3002 (American Institute of Aeronautics and Astronautics, Reston, VA, 1997).
- [15] R. Bur, B. Corbel, and J. Delery, Study of passive control in a transonic shock wave/boundary-layer interaction, *AIAA J.* **36**, 394 (1998).
- [16] V. Pasquariello, M. Grilli, S. Hickel, and N. A. Adams, Large-eddy simulation of passive shock-wave/boundary-layer interaction control, *Int. J. Heat Fluid Flow* **49**, 116 (2014).
- [17] M. Y. Ali, F. S. Alvi, R. Kumar, C. Manisankar, S. B. Verma, and L. Venkatakrishnan, Studies on the influence of steady microactuators on shock-wave/boundary-layer interaction, *AIAA J.* **51**, 2753 (2013).
- [18] S. B. Verma, C. Manisankar, and C. Raju, Control of shock unsteadiness in shock boundary-layer interaction on a compression corner using mechanical vortex generators, *Shock Waves* **22**, 327 (2012).
- [19] S. B. Verma, C. Manisankar, and P. Akshara, Control of shock-wave boundary layer interaction using steady micro-jets, *Shock Waves* **25**, 535 (2015).
- [20] D. P. Ramaswamy and A.-M. Schreyer, Control of shock-induced separation of a turbulent boundary layer using air-jet vortex generators, *AIAA J.* **59**, 927 (2021).
- [21] M. A. Eitner, Y.-J. Ahn, M. N. Musta, L. Vanstone, J. Sirohi, and N. T. Clemens, Effect of shock wave boundary layer interaction on vibratory response of a compliant panel, in *AIAA Aviation Forum*, AIAA Paper No. 2021-2493 (American Institute of Aeronautics and Astronautics, Reston, VA, 2021).
- [22] J. Poggie, *Control of Shock-Wave /Boundary-Layer Interaction Using Volumetric Energy Deposition*, AIAA Paper No. 2008-1090 (American Institute of Aeronautics and Astronautics, Reston, VA, 2008).
- [23] A. Sasoh, A. Iwakawa, T. Osuka, R. Majima, T. Tamba, and T. Sakai, *Control of Shock Wave-Boundary Layer Interaction by Repetitive Laser Energy Depositions*, AIAA Paper No. 2014-2369 (American Institute of Aeronautics and Astronautics, Reston, VA, 2014).
- [24] A. Iwakawa, T. Tamba, H. S. Pham, T. Shoda, and A. Sasoh, *Control of Shock Wave Boundary Layer Interaction using Laser Pulse Energy Depositions*, AIAA Paper No. 2015-2781 (American Institute of Aeronautics and Astronautics, Reston, VA, 2015).

- [25] A. Iwakawa, T. Tamba, H. S. Pham, T. Shoda, and A. Sasoh, *Pulse Energy Effect on Shock Wave Boundary Layer Interaction Control using Repetitive Energy Depositions*, AIAA Paper No. 2016-3342 (American Institute of Aeronautics and Astronautics, Reston, VA, 2016).
- [26] E. Caraballo, N. Webb, J. Little, J.-H. Kim, and M. Samimy, *Supersonic Inlet Flow Control Using Plasma Actuators*, AIAA Paper No. 2009-924 (American Institute of Aeronautics and Astronautics, Reston, VA, 2009).
- [27] N. Webb, C. Clifford, and M. Samimy, *Preliminary Results on Shock Wave/Boundary Layer Interaction Control Using Localized Arc Filament Plasma Actuators*, AIAA Paper No. 2011-3426 (American Institute of Aeronautics and Astronautics, Reston, VA, 2011).
- [28] N. Webb, C. Clifford, and M. Samimy, Control of oblique shock wave/boundary layer interactions using plasma actuators, *Exp. Fluids* **54**, 1545 (2013).
- [29] T. Gan, Y. Wu, Z. Sun, D. Jin, H. Song, and M. Jia, Shock wave boundary layer interaction controlled by surface arc plasma actuators, *Phys. Fluids* **30**, 055107 (2018).
- [30] M. Tang, Y. Wu, S. Guo, Z. Sun, and Z. Luo, Effect of the streamwise pulsed arc discharge array on shock wave/boundary layer interaction control, *Phys. Fluids* **32**, 076104 (2020).
- [31] M. Tang, Y. Wu, S. Guo, H. Liang, and Y. Luo, Compression ramp shock wave/boundary layer interaction control with high-frequency streamwise pulsed spark discharge array, *Phys. Fluids* **32**, 121704 (2020).
- [32] V. Narayanaswamy, L. L. Raja, and N. T. Clemens, Control of a shock/boundary-layer interaction by using a pulsed-plasma jet actuator, *AIAA J.* **50**, 246 (2012).
- [33] V. Narayanaswamy, L. L. Raja, and N. T. Clemens, Control of unsteadiness of a shock wave/turbulent boundary layer interaction by using a pulsed-plasma-jet actuator, *Phys. Fluids* **24**, 076101 (2012).
- [34] B. R. Greene, N. T. Clemens, P. Magari, and D. Micka, Control of mean separation in shock boundary layer interaction using pulsed plasma jets, *Shock Waves* **25**, 495 (2015).
- [35] K. Kinefuchi, A. Y. Starikovskiy, and R. B. Miles, Control of shock-wave/boundary-layer interaction using nanosecond-pulsed plasma actuators, *J. Propul. Power* **34**, 909 (2018).
- [36] C. Kalra, S. H. Zaidi, B. J. Alderman, R. B. Miles, and Y. V. Murty, *Magnetically Driven Surface Discharges for Shock-Wave Induced Boundary-Layer Separation Control*, AIAA Paper No. 2007-222 (American Institute of Aeronautics and Astronautics, Reston, VA, 2007).
- [37] C. S. Kalra, S. H. Zaidi, R. B. Miles, and S. O. Macheret, Shockwave-turbulent boundary layer interaction control using magnetically driven surface discharges, *Exp. Fluids* **50**, 547 (2011).
- [38] M. D. Atkinson, J. Poggie, and J. A. Camberos, Control of separated flow in a reflected shock interaction using a magnetically-accelerated surface discharge, *Phys. Fluids* **24**, 126102 (2012).
- [39] N. J. Bisek, D. P. Rizzetta, and J. Poggie, Plasma control of a turbulent shock boundary-layer interaction, *AIAA J.* **51**, 1789 (2013).
- [40] L. J. Mears, N. Arora, and F. S. Alvi, *Introducing Controlled Perturbations in a 3-D Swept Shock Boundary Layer Interaction*, AIAA Paper No. 2018-2076 (American Institute of Aeronautics and Astronautics, Reston, VA, 2018).
- [41] L. J. Mears, N. Arora, and F. S. Alvi, *Flowfield Response to Controlled Perturbations in Swept Shock/Boundary-Layer Interaction Using Unsteady Pressure-Sensitive Paint*, AIAA Paper No. 2019-0094 (American Institute of Aeronautics and Astronautics, Reston, VA, 2019).
- [42] A. Mohammed-Taifour and J. Weiss, Periodic forcing of a large turbulent separation bubble, *J. Fluid Mech.* **915**, A24 (2021).
- [43] S. Priebe, J. H. Tu, C. W. Rowley, and M. Pino Martin, Low-frequency dynamics in a shock-induced separated flow, *J. Fluid Mech.* **807**, 441 (2016).
- [44] J.-M. Chomaz, Global instabilities in spatially developing flows: Non-normality and nonlinearity, *Annu. Rev. Fluid Mech.* **37**, 357 (2005).
- [45] M. C. Adler and D. V. Gaitonde, Dynamic linear response of a shock/turbulent-boundary-layer interaction using constrained perturbations, *J. Fluid Mech.* **840**, 291 (2018).
- [46] T. Hacker, B. Yang, and G. McCartney, Empowering Faculty: A campus cyberinfrastructure strategy for research communities, *Educause Review* (2014).

- [47] D. S. Dolling and S. M. Bogdonoff, *An Experimental Investigation of the Unsteady Behavior of Blunt Fin-Induced Shock Wave Turbulent Boundary Layer Interactions*, AIAA Paper No. 1981-1287 (American Institute of Aeronautics and Astronautics, Reston, VA, 1981).
- [48] D. S. Dolling and S. M. Bogdonoff, Blunt fin-induced shock wave/turbulent boundary-layer interaction, [AIAA J. **20**, 1674 \(1982\)](#).
- [49] T. Economon, F. Palacios, S. R. Copeland, T. W. Lukaczyk, and J. J. Alonso, SU2: An open-source suite for multiphysics simulation and design, [AIAA J. **54**, 828 \(2016\)](#).
- [50] E. S. Molina, C. Spode, R. G. A. Silva, D. E. Manosalvas-Kjono, S. Nimmagadda, T. D. Economon, J. J. Alonso, and M. Righi, *Hybrid RANS/LES Calculations in SU2*, AIAA Paper No. 2017-4284 (American Institute of Aeronautics and Astronautics, Reston, VA, 2017).
- [51] M. L. Shur, P. R. Spalart, M. K. Strelets, and A. K. Travin, An enhanced version of DES with rapid transition from RANS to LES in separated flows, [Flow Turbul. Combust. **95**, 709 \(2015\)](#).
- [52] P. R. Spalart and S. R. Allmaras, A one-equation turbulence model for aerodynamic flows, in *30th Aerospace Sciences Meeting and Exhibit*, AIAA Paper No. 1992-439 (American Institute of Aeronautics and Astronautics, Reston, VA, 1992).
- [53] A. S. Deshpande, Unsteady dynamics of shock-wave boundary-layer interactions, Ph.D. thesis, Purdue University, 2021.
- [54] P. Stoica and R. Moses, *Spectral Analysis of Signals* (Pearson Prentice Hall, Upper Saddle River, NJ, 2005), Secs. 2.6.2 and 2.7.2.
- [55] M. P. Martin, S. Priebe, and C. M. Helm, *Upstream and Downstream Influence on STBLI Instability*, AIAA Paper No. 2016-3341 (American Institute of Aeronautics and Astronautics, Reston, VA, 2016).